Practicalities of BVID detection on aerospace-grade CFRP materials with optical fibre sensors

Sidney Goossens [a],*, Francis Berghmans [a], Zahra Sharif Khodaei [b], Florian Lambinet [b], Evangelos Karachalios [c], Diego Saenz-Castillo [d], Thomas Geernaert [a]

[a] Brussels Photonics (B-PHOT), Vrije Universiteit Brussel and Flanders Make, Dept. of Applied Physics and Photonics, Pleinlaan 2, B-1050 Brussels, Belgium
[b] Imperial College London, Department of Aeronautics, South Kensington Campus, Exhibition Road, SW7 2AZ London, UK
[c] Hellenic Aerospace Industry, Engineering Research Design and Development Directorate, 32009 Schimatari, Greece
[d] FIDAMC, Foundation for the Research, Development and Application of Composite Materials, Avda. Rita Levi Montalcini 29, Tecnogetafe, 28906 Getafe, Madrid, Spain

ARTICLE INFO

ABSTRACT

Several reports have recently shown the capability of optical fibre sensors for the detection of barely visible impact damage (BVID) on CFRP laminates, based on changes in the optical signal before and after impact. Although this approach was shown to work well in lab conditions, little attention has been paid so far to its practicality when considering realistic ambient conditions or to the detection range. In this work we attempt to derive BVID detection thresholds for fibre Bragg grating-based sensors, by considering standardized temperature and vibration levels for aerospace applications. To the best of our knowledge this is the first practical threshold assessment for BVID detection on aerospace-grade CFRP for such sensors. We have put our detection thresholds to the test by analysing a total of 24 BVIDs on 12 panels made from 4 different CFRP material systems and derived commendable sizes for the detection range on the different material systems.

1. Introduction

Barely visible impact damage (BVID) can have detrimental effects on carbon fibre reinforced polymer (CFRP) aerospace components. BVIDs are defined as damage caused by an impact such as a tool drop, bird hit or lightning strike, that lead to fibre or matrix cracking. The complex stacking nature of CFRP materials makes the out-of-plane direction more sensitive to impact damage. Despite the barely visible dent of about 0.3 mm left behind on the outer surface by a BVID, a substantially larger delaminated area can occur between the different plies. This delamination can grow drastically when exposed to structural loads, with possible component failure as a result.

To cope with the risks associated with BVIDs, it is crucial to detect them at an early stage. Current inspection methods rely on frequent and lengthy scanning methods, such as C-scan. However, such a periodic maintenance strategy implies long downtimes and high inspection costs [1,2]. In view of this, the use of integrated sensor networks has been proposed to facilitate a condition-based maintenance approach instead. Optical fibre sensor (OFS) networks have been heralded for that purpose. More specifically, fibre Bragg gratings (FBGs) have been claimed to provide excellent solutions for a variety of structural health monitoring (SHM) problems, owing to their low weight, immunity for electromagnetic interference and multiplexing capabilities. In addition, they can be either bonded to the surface of a composite or embedded within the material [3].

Several studies investigated the possibilities of detecting and locating an impact by directly measuring the shock wave caused by the impact with embedded [4–10] as well as with (unpackaged) surface mounted [11–24] optical fibres. This approach however requires an OFS interrogation system that continuously reads out the sensors with a high acquisition speed and should thus be on-board permanently with all regulatory and practical strings attached. Moreover, the sensors used in literature were barely tested for their compatibility with in-flight conditions such as for example structural loading or vibrations.

Alternatively, a methodology for detecting not the impact itself but the resulting BVID can allow for running on-ground diagnostics and hence also enabling condition-based maintenance. Embedded optical fibres have shown to be capable of detecting the strain redistribution due to BVIDs, cracks and delamination based on the spectral deformation of the Bragg reflection peak [25–34] or by optical path length changes as measured by distributed optical fibre sensing techniques [35,36]. Although embedded optical fibres are touted to benefit from the intrinsic protection from in-flight conditions by residing within the

---

* Corresponding author.
  E-mail address: sidney.goossens@vub.be (S. Goossens).

host material, not all composite manufacturing methods allow for optical fibre embedding. Embedded optical fibres are also challenging, if not impossible, to repair in case of failure. Furthermore, assuring the reliability of the optical connection to the optical fibre sensor through the in- and egress points at the composite component's side or top edge remains a head-breaker. Finally, concerns remain about the structural integrity and load bearing capacity of the composite material when optical fibres are integrated. These shortcomings restrict the deployment of embedded fibres in many industrial composite applications.

Surface-mounting optical fibre sensors onto the composite avoids the complications associated with embedding, while their key advantages in terms of low weight, multiplexing capability, limited cabling complexity and EMI immunity can still be exploited. A few reports have established the capability of surface mounted optical fibres to detect BVIDs. They do so either by means of vibrational or modal analysis [37–40], based on the local strain field in the vicinity of the BVID [41] or based on the spectral deformation of an FBG reflection peak [42]. So far these reports all remain at the level of lab demonstrations, and do not consider even some of the most straightforward practical considerations that may impact the assessment of such an approach in an industrial aerospace application. None of the above studies have verified the compatibility with on-ground conditions such as temperature differences or (engine) vibrations. Most studies only consider BVIDs at the exact location of the FBG sensor. Only one publication shows results for the dependence of the BVID induced strain on the distance to the FBG [41]. Furthermore, the influence of the CFRP material system on the strain measurement and on the required sensor density for accurately detecting BVIDs have also remained largely unexplored.

In this paper we attempt to address those concerns. After having previously reported on the compatibility of ruggedized FBG sensors and their installation with in-flight conditions [43], we turn our attention here to the optical fibre sensor signals that allow for BVID detection as well to quantified thresholds for the derived damage indicators that consider several practical aspects. For that purpose we equipped 4 types of highly relevant aerospace-grade CFRP material systems with in-flight compatible optical fibre sensor arrays [43]. We first exposed a total of 12 panels to standardized on-ground conditions such as temperature differences between the baseline measurement and test measurement, and the presence of aircraft engine vibrations. We investigated the detection limits that these conditions impose on the detection methodology of BVIDs. We then put the resulting thresholds to the test by performing a total of 24 calibrated impacts with different energies and on different locations and evaluating the success of the detection with two damage indicators. Finally, we estimate the size of the BVID detection range for the different material systems and damage indicators.

We structured our manuscript as follows. Section 2 briefly introduces the composite materials and elaborates on the type of optical fibre sensors and installation method. We explain the properties of a fibre Bragg grating, and its reaction to static (non-)uniform strain. We also study how these characteristics allow for detecting BVIDs and can be calibrated for standardized on-ground conditions. Section 3 elaborates on the effects on the on-ground conditions in terms of temperature and vibrations and the resulting detection thresholds. Section 4 establishes the size of the detection range within which the damage indicators that we have analysed are successful for BVID detection.

2. Materials and methods

2.1. Composite panels

Our test samples are panels fabricated from 4 different state-of-the-art aerospace CFRP materials. The material types and their stacking sequence are summarized in Table 1, and will from now on be referred to as M1 to M4. Detailed information about the materials and their

manufacturing process can be found in Appendix A: composite panel manufacturing. All panels were trimmed for obtaining the final dimensions of 225 × 300 mm, as illustrated in Fig. 1 and Fig. 2.

2.2. Fibre sensors

The fibre Bragg gratings used in this work are draw-tower-gratings (DTGs®). These FBGs are inscribed during the actual drawing of the optical fibre itself, and before applying any coating, which results in excellent strength and fatigue characteristics [48,49]. The fibre is coated by a layer of Ormocer® and packaged with glass fibre reinforced polymer (GFRP) and an 0.2mm outer jacket of high-density polyethylene (HDPE) which yields a wire-like sensor cable with a total outer diameter of 1.0 mm. The DTGs® used here had a length of 8 mm and a reflectivity of about 30 %. They have been purchased from FBGS International [50].

The fibres were bonded to the CFRP by encapsulating them over the whole length with a layer of HBM X120 two-component epoxy adhesive designed for optical fibres [51]. This is shown on M1/M4 and M3 in Fig. 3 and on M2 in Fig. 1. The strain measurement wires were annealed in 3 temperature cycles from RT to 120 ℃ prior to their installation to guarantee stable FBG operation at operational temperatures (up to 85 °C) [43,62,63]. Both the sensor as well as the installation method have been previously tested to survive standardized in-flight conditions for temperature, pressure, humidity, fluid susceptibility, vibrations and tensile fatigue, as described in more detail in [43]. We showed that in-flight temperature cycling (−65 ± 85 °C) had no noticeable effect on the quality of the Bragg peak shape [43].

The fibres were mounted in a cross formation onto the CFRP, with a vertically and horizontally oriented fibre, as also illustrated in Fig. 2. This orthogonal configuration allowed locating BVIDs with a relatively small number of sensors. Each fibre holds 6 wavelength-multiplexed FBGs with a centre to centre distance of 26 mm. The spectrum of the FBG array on a horizontally mounted fibre before and after installation on an M1 panel is shown in Fig. 4. The 6 Bragg peaks can clearly be identified. They showed a wavelength shift of 158.8 ± 3.6 pm due to the applied prestrain during installation. The robust packaging and optimized installation method ensured that the Bragg peak shape, side-lobe suppression and signal-to-noise ratio remain at an adequate level for further measurements.

2.3. FBG-based damage indicators

A fibre Bragg grating is a periodic refractive index modulation of typically a few millimetres long in the core of an optical fibre, which reflects a narrow spectral bandwidth of light centred around the Bragg wavelength λ_B given by Eq. (1) [52,53]:

$$\lambda_B = 2n_{eff}\Lambda \tag{1}$$

λ_B depends on the effective refractive index n_{eff} and the physical period Λ of the refractive index modulation. Whenever a uniform strain or temperature difference is applied to the FBG, n_{eff} and Λ will change, and therefore λ_B will shift to a lower or higher wavelength [54]. However, when a non-uniform strain is present over the length of the grating, the reflected Bragg spectrum will also deform [6,8,9,25–33,42]. This is illustrated in an exaggerated manner for the sake of clarity in Fig. 5.

If a CFRP structure is damaged by a BVID, the strain field around the impact location will change. An FBG located within the area of the strain redistribution will be exposed to that (non-)uniform strain. This strain change can be observed by comparing the Bragg wavelength shift ($\Delta\lambda_B$) and the Pearson correlation coefficient (ρ) between the pristine spectrum and the spectrum after impact. These two figures of merit are therefore proposed as damage indicators that will serve the detection of the BVIDs.

Table 1
Overview of the four types of CFRP materials.

Ref.	CFRP type	Material	Stacking sequence	Thickness
M1	UD thermoset prepreg	M21/194/34%/T800S [44]	[+45/−45/0₂/90/0]s	2.21 mm
M2	Dry fibre (NCF) + resin	U-C-PB-209 g/m²-1220 mm and PRISM EP2400 resin [45,46]	[+45/90/−45/0/+45/0/0/−45]s	3.31 mm
M3	UD thermoplastic prepreg	Tenax®-E TPCL PEEK-HTA40 [47]	[0/90/+45/−45/0/90/+45/−45/0]	2.79 mm
M4	M1 + FXPly Carbon Nanotubes	M21/194/34%/T800S + CNTs [44]	[+45/−45/0₂/90/0]s	2.32 mm
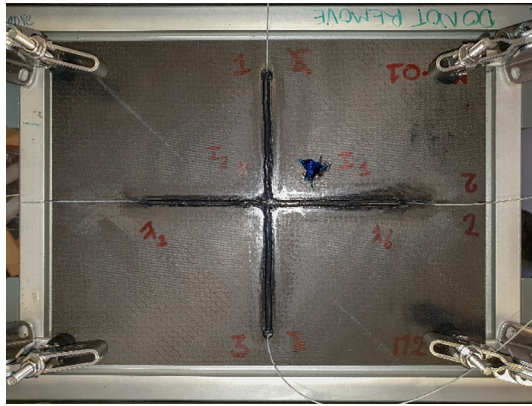
Fig. 1. Photograph of an M2 panel clamped into the impacting frame, showing the surface mounted fibres and impact locations I1 and I2.
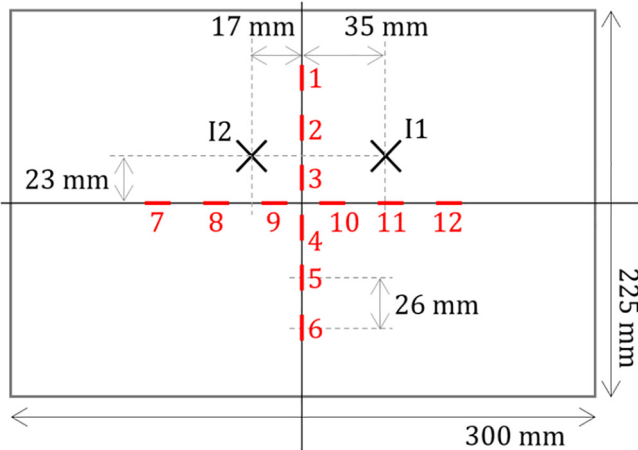

Fig. 2. Dimensions of the CFRP panels with bonded optical fibres with the FBGs locations marked in red and impact location by black crosses labeled I1 and I2.

Fig. 4. Reflected power spectrum of 6 wavelength-multiplexed FBGs on the horizontally mounted fibre before and after installation on a M1 panel."

To determine λ_B we performed a Gaussian fit on the linear spectral data with the squared amplitude as weights in the typical Bragg peak bandwidth: a 200 pm window centring the maximum of the Bragg peak.

The Pearson correlation coefficient (2) quantifies the cross-correlation between respective datasets x_i and y_i ($i = 1, \cdots, n$) as given by Eq. (2). Note that the correlation coefficient will depend on the wavelength window that is studied, as well as the interrogator used for obtaining the spectra (amount of datapoints n, presence of measurement noise…). In this work we used a 200 pm window centring λ_B, with a 0.1 pm resolution after interpolating the raw data if necessary.

$$\rho = \frac{\sum_{i=1}^{n}(x_i - \overline{x})(y_i - \overline{y})}{\sqrt{\sum_{i=1}^{n}(x_i - \overline{x})^2}\sqrt{\sum_{i=1}^{n}(y_i - \overline{y})^2}} \qquad (2)$$

If the spectra before and after impact show a $\Delta\lambda_B = 0$ and $\rho = 100\%$, no strain change is observed. If, however, they show a $\Delta\lambda_B \neq 0$ and/or $\rho < 100\%$, a uniform strain and/or non-uniform strain are respectively acting on the FBG.

In this work, the spectra were acquired in reflection with two interrogation methods. The first was a custom-built setup based on a Santec TSL-710 tunable laser source [55] and a Thorlabs PDA20CS InGaAs photodiode [56] sampled by a TiePie Handiscope HS5 data acquisition
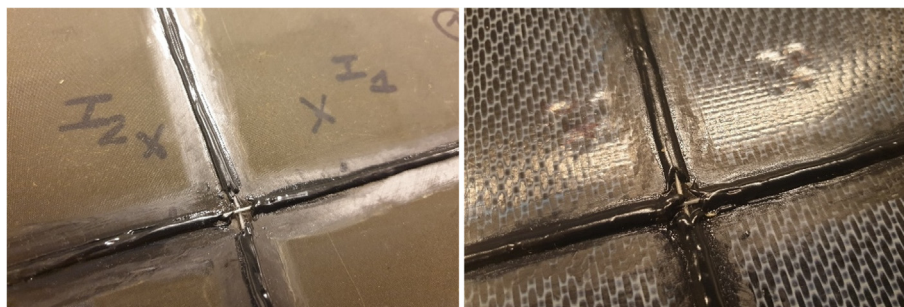

Fig. 3. Centre photograph of an M1 panel (left) and an M3 panel (right) showing the surface mounted fibre configuration and BVID indentation at the marked impact locations.
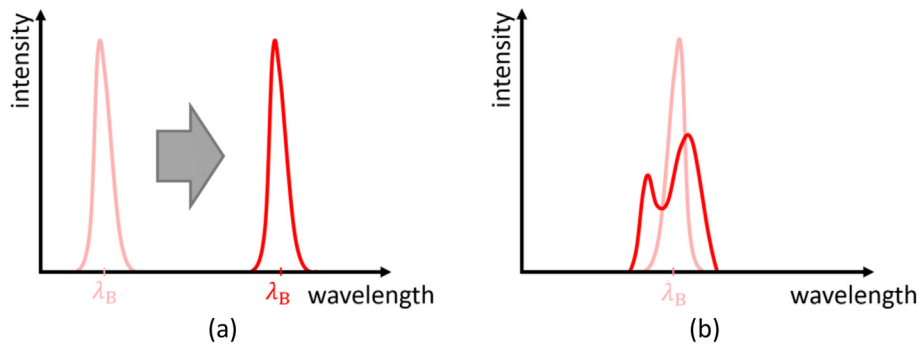
Fig. 5. Schematic representation of (a) uniform strain acting along the length of an FBG, yielding a wavelength shift and (b) an increase in non-uniform strain yielding a deformation (exaggerated) of the Bragg spectrum. the reflection spectrum in the unstrained situation is in light red and the strained situation is in dark red.

system [57], reaching a wavelength resolution of 0.1 pm. The second was a Micron Optics sm125-500 4-channel interrogator with a wavelength resolution of 5 pm [58].

2.4. Temperature and vibration analysis

Changes of the two damage indicator values may not only originate from actual damage but could also be attributed to changing ambient conditions. We therefore evaluated the effect of temperature and vibrations, representative for on-ground conditions, on these damage indicators. The Standardized Ground Survival Temperatures for a regional aircraft are −40 and +50 °C [59], and thus our methodology was tested for this temperature range.

Two instrumented M1 and two instrumented M3 panels were placed in a Thermal Vacuum Chamber J2235 by Temperature Applied Sciences [60]. The temperature was increased from −40 °C to +50 °C in steps of 5 °C with dwell times of 45 min to ensure a stabilized temperature when performing the spectral measurements. The temperature profile obtained by the thermocouple of the environmental chamber can be seen in Fig. 6, and the spectra were recorded 4 times in the last 15 min of each step.

To represent the vibrations associated with running aircraft engines, we attached one M4 panel to a shaker and applied a Standard Vibration Test [61] frequency spectrum as can be seen in Fig. 7. The spectra of the fibres were acquired for 60 s both in the absence and in the presence of the standardized vibrations.

3. Results and discussion for threshold definition

When a component is checked for damage, the baseline may have been acquired at environmental conditions that differ substantially from the actual test situation. The temperature may for example differ and since FBG sensors are cross-sensitive to strain and temperature changes, this temperature difference must be corrected for. To do so, we extract the temperature sensitivity of the installed FBG sensors and use that data to correct the Bragg wavelength for that part of its wavelength shift that is purely due to the temperature difference. The corrected data can then be considered compensated for the temperature difference. However, the precision of that compensation will determine the practical detection limit of wavelength shifts that originate from BVIDs if any, and thus constitute a threshold value for the damage indicator based on the Bragg wavelength.

3.1. Temperature analysis

To assess the precision of the temperature compensation, two sensorized M1 panels and two sensorized M3 panels were subjected to the temperature profile introduced in Section 2.4. For each individual sensor, the Bragg wavelength was determined and for that data both a lin-
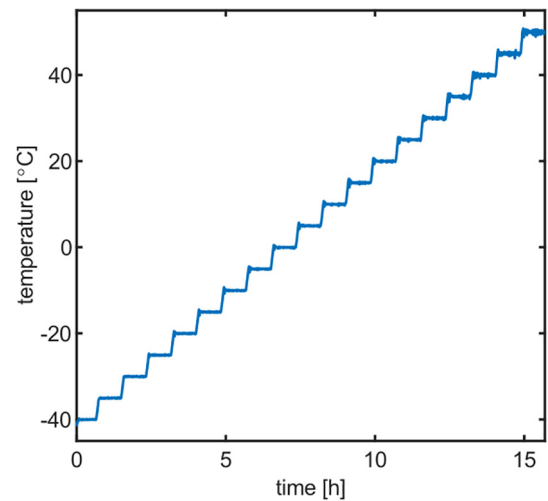

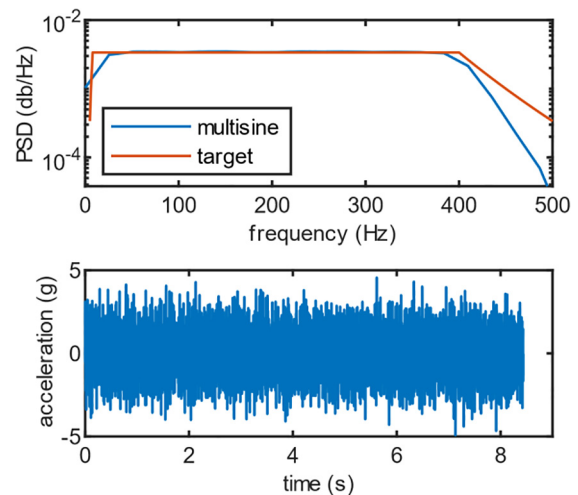**Fig. 6.** Temperature profile of the environmental chamber.

Fig. 7. Power spectral density function (top) and (portion of the) acceleration profile (bottom) of the vibration signal.

ear and quadratic fit were applied, as shown for one sensor on an M1 panel in Fig. 8.

The linear fit allowed assessing the temperature sensitivity, which was 10.62 ± 0.98 pm/°C for the fiber sensors in the horizontal direc-

tion and 15.47 ± 1.31 pm/°C in the vertical direction for M1 with $R^2 = 99.50 \pm 0.57\%$, and 13.85 ± 0.77 pm/°C in the horizontal and 13.88 ± 0.89 pm/°C in het vertical direction of M3 with $R^2 = 99.74 \pm 0.16\%$. The standard deviation of the sensitivities and direction dependence illustrate that individual temperature characterization of each FBG sensor is meaningful. Note that a significant improvement of the fit is achieved when opting for a quadratic curve, as shown in the example of Fig. 8. The average R^2-value of all 48 sensors for their quadratic fit was $99.96 \pm 0.06\%$.

With these sensor-specific quadratic equations we investigated the effect of temperature compensation, in the following steps:

1. acquire the Bragg wavelength of all 12 sensors on the panel at the unknown temperature.
2. use their individual quadratic fit to obtain a temperature value per sensor.
3. calculate the median temperature of the 12 sensors.
4. use the inverse quadratic relation to reconstruct the Bragg wavelength of every sensor for this median temperature.
5. subtract the measured Bragg wavelength from the reconstructed Bragg wavelength.

This reconstruction was performed for all 48 sensors at all temperature levels of the climate chamber data set. The differences of every reconstructed Bragg wavelength with the actual measured Bragg wavelength were combined per material and are shown in a histogram for M1 in Fig. 9 and for M3 in Fig. 10, respectively.

We observe that compensating for temperature differences yields mean deviations from the actual Bragg wavelength of 0.05 ± 4.78 pm for M1 and 0.31 ± 5.59 pm. Considering a near certainty confidence interval of 99.7%, compensating for temperature imposes a lower threshold (τ) on the $\Delta\lambda_B$ damage indicator of $\boldsymbol{\tau_T(\Delta\lambda_B) = 14.3}$**pm for M1** and $\boldsymbol{\tau_T(\Delta\lambda_B) = 16.8}$**pm for M3**.

One M1 panel was additionally tested in 5 temperature cycles from ~50 °C to room temperature while the Bragg wavelength of the 12 surface mounted FBG sensors as well as the panel's temperature were recorded. For every cycle a 2nd degree polynomial fit of λ_B in function of temperature was performed. We then reconstructed the Bragg wavelength of every sensor based on the median temperature measured on the panel at all measurements of the 5th cycle. We did so by sequentially using the fit parameters obtained in the previous 4 cycles. We observed that the variance on the error between the reconstructed Bragg wavelengths and the measured Bragg wavelengths decreases exponentially with the cycle number of which the fit parameters were
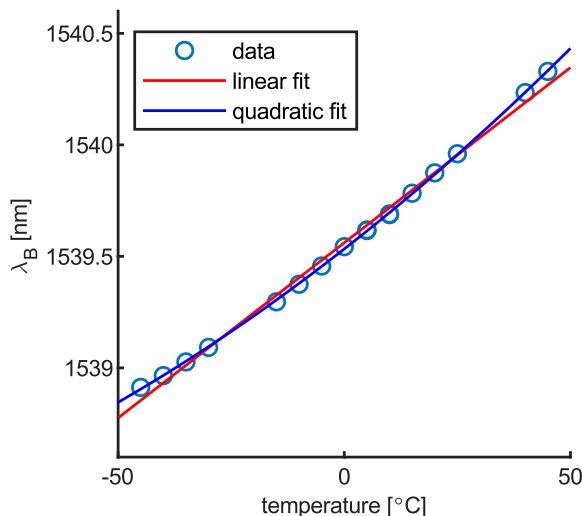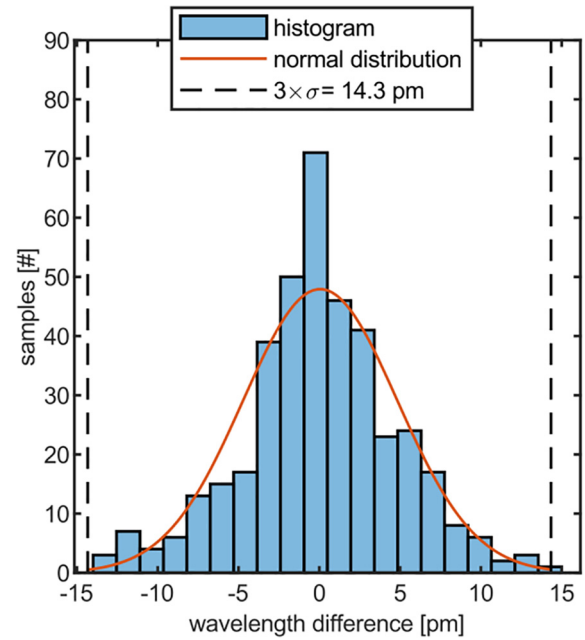

Fig. 9. Histogram and fitted normal distribution of the difference values between measured and temperature reconstructed Bragg wavelengths for M1.
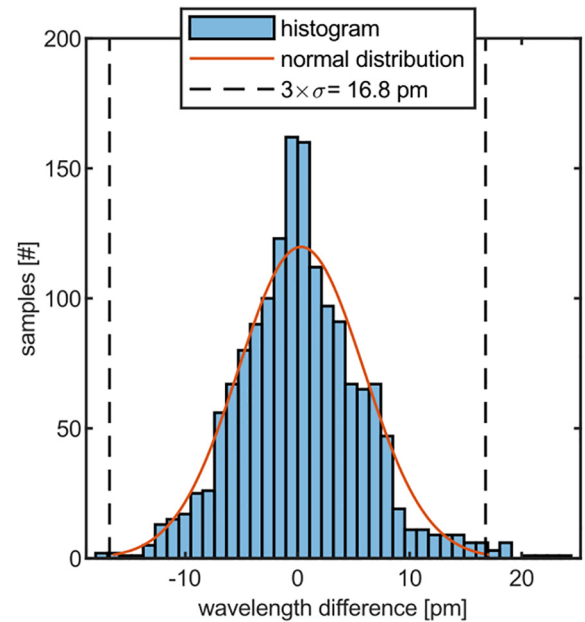

Fig. 10. Histogram and fitted normal distribution of the difference values between measured and temperature reconstructed Bragg wavelengths for M3.

used, as shown in Fig. 11. This shows that the repeatability of the temperature response increases by temperature cycling, as the variance on the error can be decreased below 1 pm. In practice the repeatability may depend on the material system, optical fibre packaging and mounting adhesive, mounting direction, stiffening of the component, etc. Since temperature cycling of a large instrumented component will possibly not always be feasible, we continue with the thresholds obtained in the previous analysis of $\tau_T(\Delta\lambda_B) = 14.3$pm for M1 and $\tau_T(\Delta\lambda_B) = 16.8$ pm for M3 as "worst case scenario" values.

A similar analysis was performed for the second damage indicator ρ. In this analysis the Bragg peak at the start of the temperature profile at -45 °C was correlated with each Bragg peak at all other tempera-

Fig. 8. Bragg wavelengths of an FBG sensor on an M1 panel in function of temperature with a linear and quadratic fit.

tures. All correlation coefficients were combined per material and the histogram and gamma distribution of the $1 - \rho$ values can be found in Fig. 12 and Fig. 13 for M1 and M3 respectively.

Taking into account a 99.7% confidence interval on the cumulative distribution function (CDF), this results in a detection threshold of $\boldsymbol{\tau_T}(1 - \boldsymbol{\rho}) = \mathbf{1.29\%}$ **for M1** and $\boldsymbol{\tau_T}(1 - \boldsymbol{\rho}) = \mathbf{1.34\%}$ **for M3**.

3.2. Vibration analysis and measurement repeatability

To investigate the effect of on-ground aircraft vibration on the acquisition of the damage indicators, one M4 panel was subjected to the standardized acceleration profile of Fig. 7, while the spectra of the 12 Bragg peaks were acquired at 2 Hz for 60 sec. In order to investigate the spread of the Bragg wavelength, a linear trend was removed from the Bragg wavelength signal for every sensor, and the variation of the sensor was analysed. This is depicted for one of the 12 FBGs in Fig. 14, where the Bragg wavelength in function of time during vibrations is shown in the top graph, and the detrended signal in the bottom graph. The detrended signals of all 12 sensors were combined and the distribution on the signals with and without vibrations can be seen in Fig. 16.

From Fig. 16 we can observe that there is a variation present on the measurement and determination of the damage indicator of up to a few pm. This is the case in the presence, but also in the absence of vibrations, with a slightly larger variance in case of vibrations. Taking again a confidence interval of 99.7%, this results in a detection threshold of $\boldsymbol{\tau_{vb}}(\Delta\lambda_B) = \mathbf{2.9\ pm}$. We performed similar repeatability tests in the absence of vibrations, but at elevated temperatures of 42 ℃ and 54 ℃ We obtained the Bragg wavelength of the 12 sensors on 1 M1 panel at 2 Hz for 1 min and determined the confidence interval around λ_B as $3 \cdot \sigma = 2.1$ pm at 42 ℃ and $3 \cdot \sigma = 1.9$ pm at 54 ℃, which agree with the spread at RT in the absence of vibrations.

Similarly, we correlated all Bragg peaks with those of the first spectrum at the start of the measurement. An overlay of 120 Bragg peak measurements of one FBG can be seen in Fig. 15 in the absence (top) and presence (bottom) of vibrations. The histograms and corresponding gamma distributions of the $1 - \rho$ values for all FBGs can be observed in Fig. 17. The CDF confidence bound of 99.7% is slightly higher in the absence of vibrations, with a value of $\boldsymbol{\tau_{vb}}(1 - \boldsymbol{\rho}) = \mathbf{1.00\%}$. This means the presence of on-ground vibrations has only a minor effect on ρ.

3.3. Overall damage indicator thresholds

The combined effect of temperature and vibration ($\tau_T + \tau_{vb}$) impose a lower detection limit on the damage indicators $\Delta\lambda_B$ and ρ, being
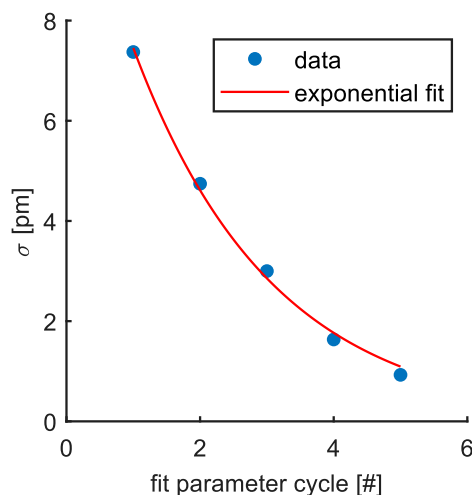

Fig. 11. Variance on the difference between the measured and the reconstructed Bragg wavelengths during annealing cycles.
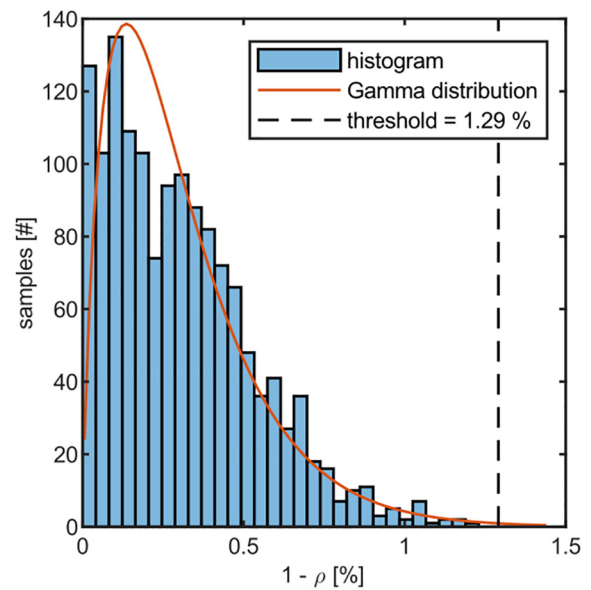

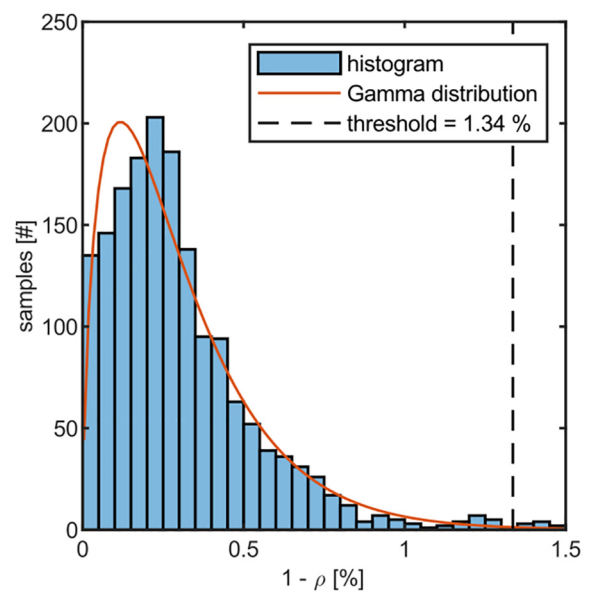**Fig. 12.** Histogram and gamma distribution of the correlation coefficients at all temperature differences for M1.

Fig. 13. Histogram and gamma distribution of the correlation coefficients at all temperature differences for M3.

$\boldsymbol{\tau}(\Delta\lambda_B) = \mathbf{17.2pm}$ **and** $\boldsymbol{\tau}(\rho) = \mathbf{2.29\%}$ **for M1** and $\boldsymbol{\tau}(\Delta\lambda_B) = \mathbf{19.7pm}$ **and** $\boldsymbol{\tau}(\rho) = \mathbf{2.34\ \%}$ **for M3**. This means a BVID can only be detected if the damage indicator surpasses these thresholds. If not, the change in the damage indicator could have possibly occurred due to environmental conditions. In the next section we will put these thresholds to the test in a systematic way by performing calibrated impacts on sensorized panels and obtaining the damage indicators after each BVID.

4. Results and discussion for damage detection

In this section we investigate the repeatability of identical BVID impact scenarios and the influence of CFRP material system, distance between the BVID's centre and the optical fibre sensor array and impact energy. We performed a total of 24 impacts on 12 CFRP panels from the materials M1 to M4.
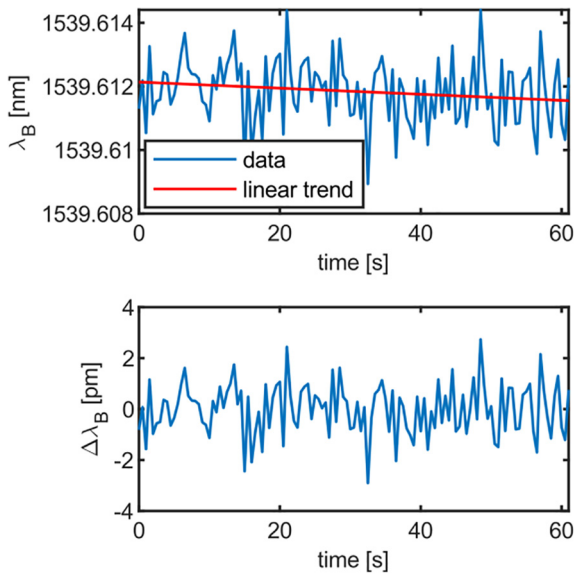
Fig. 14. Bragg wavelength of 1 FBG during vibration (top), and variation on that Bragg wavelength with linear trend removed (bottom).
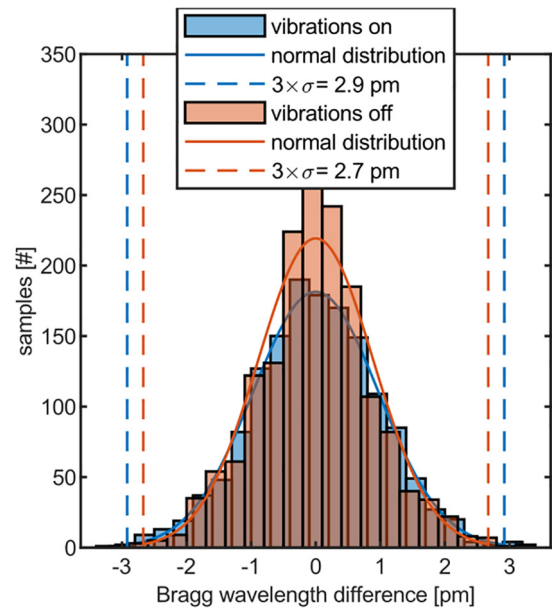

Fig. 16. Histogram and normal distribution of the Bragg wavelength variation with vibrations on and off.
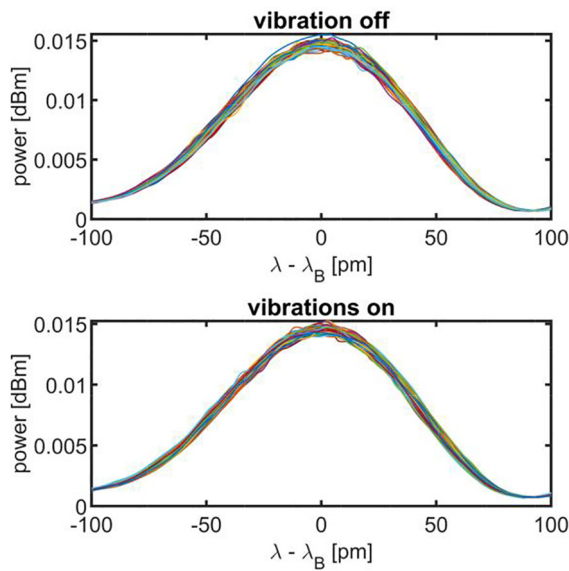

Fig. 15. 120 correlated Bragg peaks of 1 FBG with vibrations off (top) and vibration on (bottom).

Fig. 17. Histogram and gamma distribution of the correlation coefficient with vibrations on and off.

4.1. Impact method

The panels were clamped in a frame as shown in Fig. 1 and impacted by an INSTRON CEAST 9350 Drop Tower Impact System. The impact energies were experimentally calibrated beforehand for a desired BVID indentation without visible impact damage. The size of the delamination of each BVID was determined via analysis of the impact location with a DolphiCam CF08 handheld C-scan with a sensing area of 33×33 mm and 124×124 transducer elements [64].

The results of the calibrated impact energies are summarized in Fig. 18. Note that for M3, 4 impacts close to each other were needed to create a BVID with the desired delamination and indentation. Each panel was impacted at two different locations (I1 and I2), as illustrated on Fig. 2, with the same impact energy. A detailed image of the BVIDs on an M1 panel and an M3 panel can be observed in Fig. 3 left and Fig. 3 right respectively. For each combination of material and impact energy, 2 panels were tested, yielding 4 BVIDs per scenario. Fig. 18
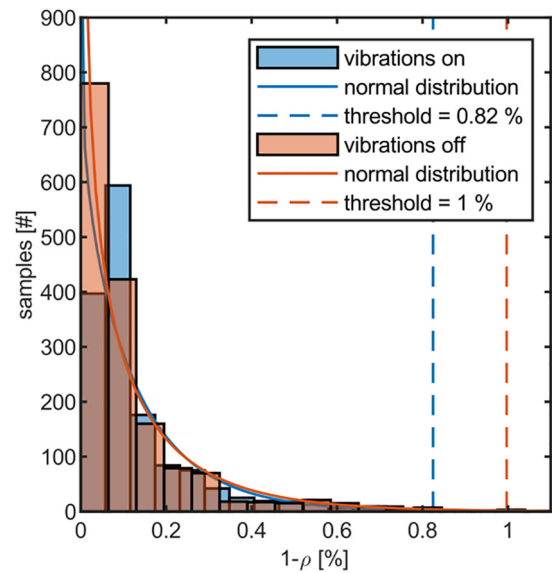
also shows the average BVID area obtained from the C-scan data of these 4 similar impacts which were between $109 \pm 19 \, \text{mm}^2$ for M1 at 16 J and $304 \pm 42 \, \text{mm}^2$ for M3 at 16 J. Fig. 19 shows an example C-scan reconstruction in 2D of a 16 J impact on M1 creating a 111 mm^2 BVID. An ellipse (also visible in Fig. 7) was fit to determine the area of each BVID.

4.2. Detection range

In this section we will estimate the size of the area in which BVID detection can be successfully carried out, depending on the material system and considering the previously derived thresholds for M1 and M3. Every panel was impacted consecutively at locations I1 and I2, as indicated in Fig. 2. For M2 and M4, one impact energy was used to create the BVID, and for M1 and M3 two different energies were investigated. For each impact energy, two panels were impacted,

resulting in 2 panels for M2 and M4 and 4 panels for M1 and M3. We obtained the damage indicators by comparing the spectra acquired prior to installing the panel in and after removing it from the impact tower. Fig. 20 shows the damage indicators for all impacts on the M1 panels. The left graphs show $|\Delta\lambda_B|$ and the right graphs show $1 - \rho$. In the top graphs, the damage indicators are shown for the BVID at location I1. The bottom graphs show the damage indicators for the BVID at I2. The thresholds $\tau(\Delta\lambda_B) = 17.2$pm and $\tau(\rho) = 2.29\%$ are displayed with dashed vertical lines. Similar figures for materials M2 to M4 can be found in Figs. B.1–B.3 in Appendix B: damage indicators for materials M2, M3 and M4.

From the figures, it can be observed that the sensors closest to the BVID show the highest damage indicator values (as expected): sensor 2 and 3 and sensor 10 and 11 for I1 and sensor 2 and 3, and 8 and 9 for I2. For all materials, impact I2 was consistently detected with the wavelength shift damage indicator. This impact location (17 mm from the vertical fibre) is the closest to the sensor array between sensor 2 and 3.

The BVID at location I1, at 35 mm from the vertical fibre and 23 mm from the horizontal fibre, was not always detected. The wavelength shift damage indicator was successful for all BVIDs on M3 but only for the higher impact energy for M1. For M3 the BVID was detected by the horizontal as well as the vertical fibre (35 mm), but for M1 only by the sensors of the vertical fibre (23 mm).

For the wavelength shift damage indicator $\Delta\lambda_B$, we conclude that surface mounted optical fibre sensors have a BVID detection range of up to **17 - 23 mm on the studied thermoset and LRI material systems**, and more than **35 mm on the considered thermoplastic material system**.

Considering the correlation coefficient $1 - \rho$ in the right panels of Fig. 20, it can be observed that all sensors are below the threshold of 2.29 %, except for the fourth panel (purple graph). The reason is that for this particular panel the second impact was not performed at a distance of 17 mm from the vertical fibre, but directly under the vertical fibre in between sensor 2 and 3. This yielded results of $1 - \rho = 10.27\%$ and $|\Delta\lambda_B| = 1676$pm for sensor 2 and $1 - \rho = 9.83\%$ and $|\Delta\lambda_B| = 741$pm for sensor 3.

The spectra of the first 3 sensors before and after the 20 J BVID at location I2 can be observed in Fig. 21. Although wavelength shifts of 200 pm can be clearly observed, the shape of the peaks doesn't change noticeably, yielding subthreshold $1 - \rho$ values. Fig. 22 shows the spectra before and after the BVID directly under the vertical fibre, and here
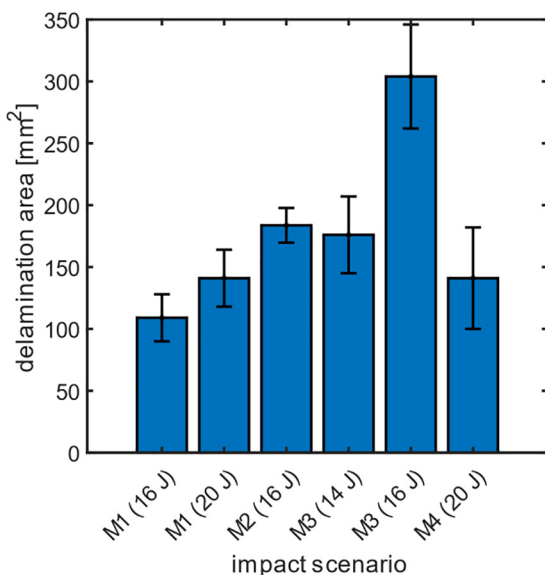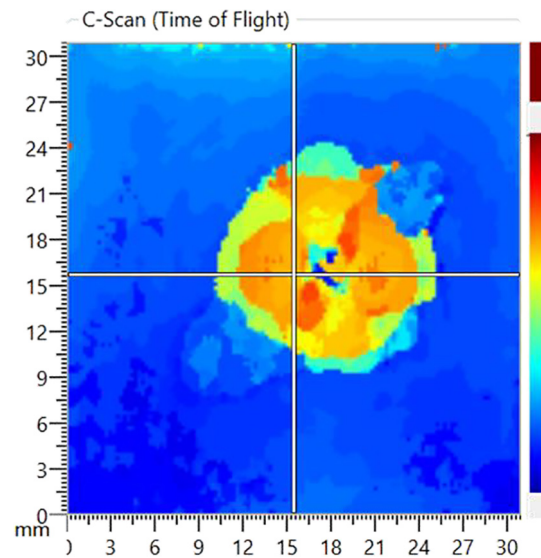

Fig. 19. C-scan data reconstruction in 2D of an example BVID of 111 mm^2 on M1 (16 J) showing in dashed line the ellipse used for deriving the BVID's area.

a clear distortion in the spectrum is observable, yielding $1 - \rho$ values of about 10%. This suggests that only a BVID with delamination extending under an optical fibre sensor array can be observed by a distortion in the spectrum with the correlation coefficient. The average BVID delamination area for all materials is 187 ± 66 mm^2 (see Fig. 18), which implies a delamination radius of 7.7 ± 4.6 mm, if we assume a circular BVID. This suggests a minimum detection distance of the same magnitude between the fibre sensor array and the BVID's centre.

The correlation coefficient damage indicators for the materials M2, M3 and M4 displayed in the right panels of Figs. B.1–B.3 respectively, show a similar result for BVIDs at 17 mm. Only 3 individual sensors pass the threshold.

Although a clear peak deformation takes place, suggesting that the correlation coefficient can indeed be used for the detection of BVIDs, we showed that this is only possible for an impact at 7.7 ± 4.6 from the fibre sensor array, as at 17 mm[6,8,9,25–33,42], we dare to question its appropriateness for larger components.

5. Conclusion

In this work we demonstrated the practical implications of BVID detection on aerospace-grade CFRP materials with surface mounted optical fibre Bragg grating sensors. In contrast to most studies in literature, we performed an investigation on the effects of standardized on-ground aircraft conditions on the detection threshold of the damage indicators: the Bragg wavelength shift and the Pearson correlation coefficient, which quantifies the change in peak shape. For our experiments, we used 4 state-of-the-art aerospace-grade CFRP material systems: a thermoset M1, a dry fibre and liquid resin (LRI) M2, a thermoplastic M3 and a CNT-infused thermoset M4.

We performed a state-of-the-art temperature calibration of the surface mounted sensors in a standardized on-ground temperature range of -45 to $+50$ °C, and extracted quadratic fits for each sensor. Compensating for the difference with this quadratic trend yields differences with the measured Bragg wavelengths which have a 99.7 % confidence bound of 14.3 pm for M1 and 16.8 pm for M3. Similar observations were made for the correlation coefficient, with a confidence bound of 1.29 % for thermoset and 1.34% for thermoplastic.

The presence of standardized on-ground vibrations and measurement noise adds a variation of 1 pm to the wavelength shift and
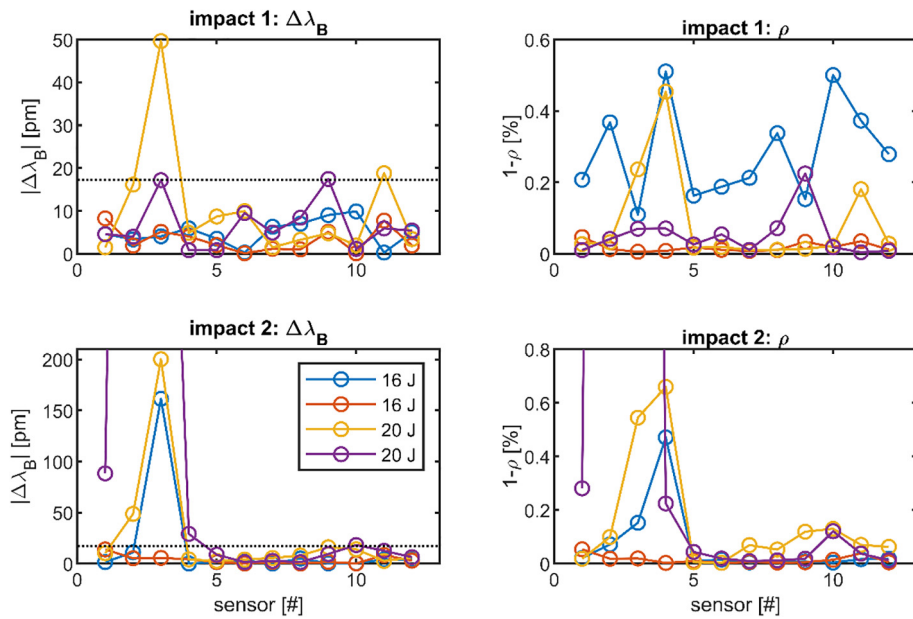

Fig. 18. Average delamination area and standard deviation of the BVIDs per impact scenario.

Fig. 20. Damage indicators for the BVIDs on M1: wavelength shift (left) and correlation coefficient (right) for impact 1 (top), impact 2 (bottom). The damage indicators for different panels are represented by different colours.
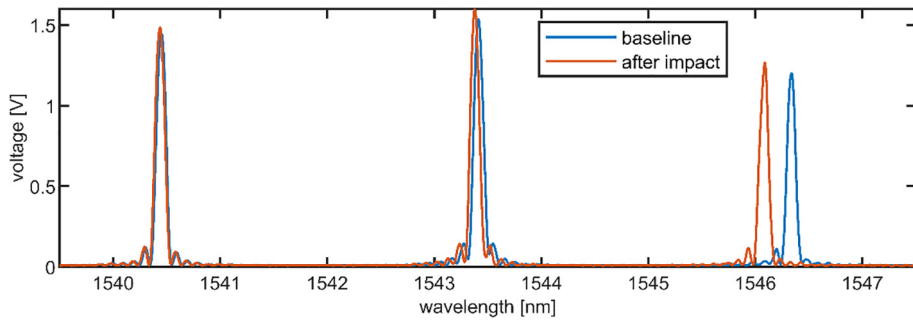

Fig. 21. Spectrum of sensors 1 to 3 for the 20 J impact at location I2 on M1.
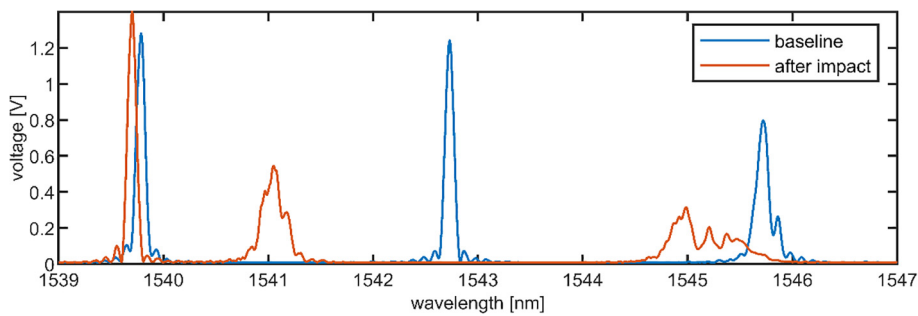

Fig. 22. Spectrum of sensors 1 to 3 for the 20 J impact directly under the vertical fibre on M1.

1.00 % to the correlation coefficient for a confidence interval of 99.7 %. The combination of the effects of temperature compensation and the presence of vibration and/or measurement noise results in an overall detection threshold of $\tau(\Delta\lambda_B) = 17.2$ pm for M1 and 19.3 pm for M3 and $\tau(\rho) = 2.29$ % for M1 and 2.34 % for M3.

To put these thresholds to the test, we created a total of 24 BVIDs on 12 panels from 4 materials. We concluded that with the wavelength shift damage indicator, the BVIDs could be detected up to a distance to the fibre array of 17 – 23 mm for M1, M4 and M2 and more than 35 mm for M3. In line with previous studies, BVIDs with a delamination reaching under the fibre sensor array yield a clearly visible peak distortion and a correlation coefficient damage indicator that surpasses the preestablished threshold. However, this implies a detection distance of only 7.7 ± 4.6 mm.

This shows that surface mounted optical fibre sensors can be used to monitor BVIDs in regions with widths up to 34 to 46 mm for thermoset and LRI, and more than 70 mm for thermoplastic material systems, considering the wavelength shift thresholds. These values can be considered as a practical recommendation for the sensor spacing. BVID detection on larger components can therefore be considered with a sensor density respecting these detection ranges.

To the best of our knowledge, this is the first demonstration that considers practical aspects for on-ground detection of BVIDs on aerospace-grade CFRP material systems using FBG-based sensors. We hope that this work contributes to increasing the technology readiness level for optical fibre sensor-based damage detection in the demanding application field of aerospace.

6. Data availability

The raw data required to reproduce these findings are available to download from https://doi.org/10.17632/p858yck56r.1 [65]. The processed data required to reproduce these findings are available to download from https://doi.org/10.17632/p858yck56r.1#file-492cec5b-c6a4-49fe-a7f1-0b6ad83da122 [65].

Declaration of Competing Interest

The authors declare that they have no known competing financial interests or personal relationships that could have appeared to influence the work reported in this paper.

Appendix A. Composite panel manufacturing

The material referred to as M1 is M21/194/34%/T800S, a unidirectional prepreg purchased from HEXCEL [44]. The panels have been manufactured by using a typical autoclave process: hand layup and a debulking operation every 4 consecutive plies followed by vacuum bagging and curing inside an autoclave at 180 °C and 7 bar. The panels had a stacking sequence of $[+45/-45/0_2/90/0]_s$ and an eventual thickness of 2.21 mm. Fig. 3 (left) shows the centre view of an M1 panel.

M2 is a combination of dry non crimp fabric (NCF) and a separate resin cured at high temperature. The fabric is the U-C-PB-209 g/m²-1220 mm manufactured by SAERTEX [45] (TENAX-E IMS65 E23 24 K with EP7702 (CYTEC Proprietary binder) and PES [Polyester] 48 dtex SC stitching) and the resin is the PRISM EP2400 manufactured by CYTEC [46]. The M2 panels were manufactured by liquid resin infusion (LRI) under vacuum. The stacking sequence was $[+45/90/-45/0/+45/0/0/-45]_s$ yielding a panel thickness of 3.10 mm.

For the manufacturing of thermoplastic composite panels referred to as M3, the material Tenax® TPCL PEEK-4-40-HTA40 3 K supplied by TOHO-TENAX was selected [47]. The material consisted of a CF/PEEK fabric 5HS (5 harness satin) with 0.31 mm nominal thickness per ply, 40 % of resin weight fraction and a fiber areal weight (FAW) of 285 gsm. The stacking sequence of the thermoplastic panels was $[0/90/45/-45/0/90/-45/45/0]$, resulting in a final panel nominal thickness of 2.79 mm. The panels were trimmed from larger laminates manufactured in a hot-plate press following a compression moulding process. The laminate was first stacked by hand and located into a metallic frame which acted as material retainer. Two polyimide sheets with release agent were placed at both sides of the laminate. Two metallic caul plates were also used for a proper flat surface finish. The consolidation cycle consisted of a heating ramp at approximately 2 °C/min up to a consolidation dwell of 30 min at 400 ± 10 °C with an applied pressure of 1 MPa. Fig. 3 (right) shows the centre view of an M3 panel.

The M4 material is the same as the M1 material but injected with carbon nanotubes (CNTs) by a treatment service using FXPly technology to increase impact resistance and for advanced electrical properties like EM shielding. The stacking sequence is the same as for M1 and the nominal thickness resulted in 2.32 mm.

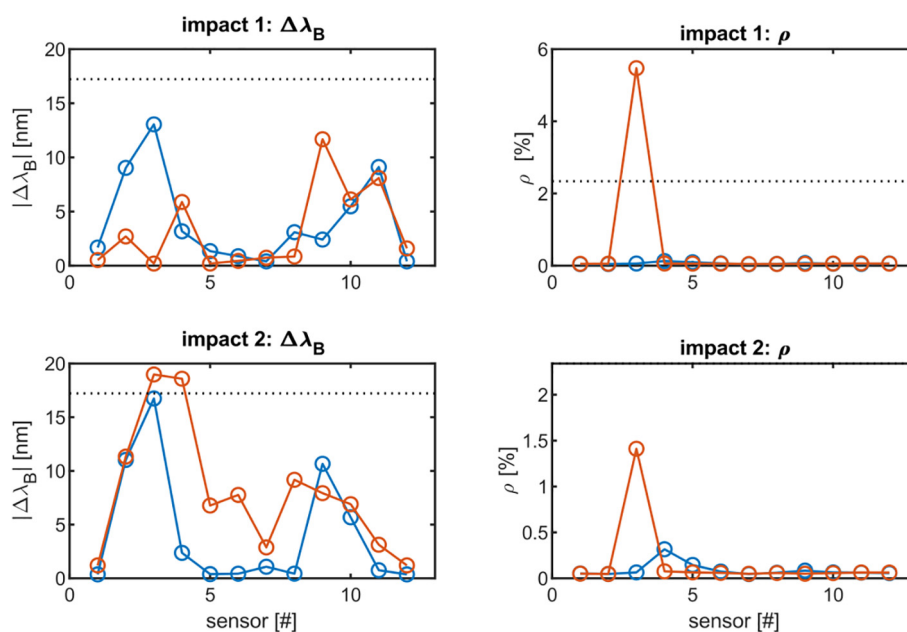## Appendix B. Damage indicators for materials M2, M3 and M4

Fig. B.1. Damage indicators for the BVIDs on M2: wavelength shift (left) and correlation coefficient (right) for impact 2 (top), impact 1 (bottom). The damage indicators for different panels are represented by different colours.

Fig. B.2. Damage indicators for the BVIDs on M3: wavelength shift (left) and correlation coefficient (right) for impact 1 (top), impact 2 (bottom). The damage indicators for different panels are represented by different colours.

Fig. B.3. Damage indicators for the BVIDs on M4: wavelength shift (left) and correlation coefficient (right) for impact 1 (top), impact 2 (bottom). The damage indicators for different panels are represented by different colours.
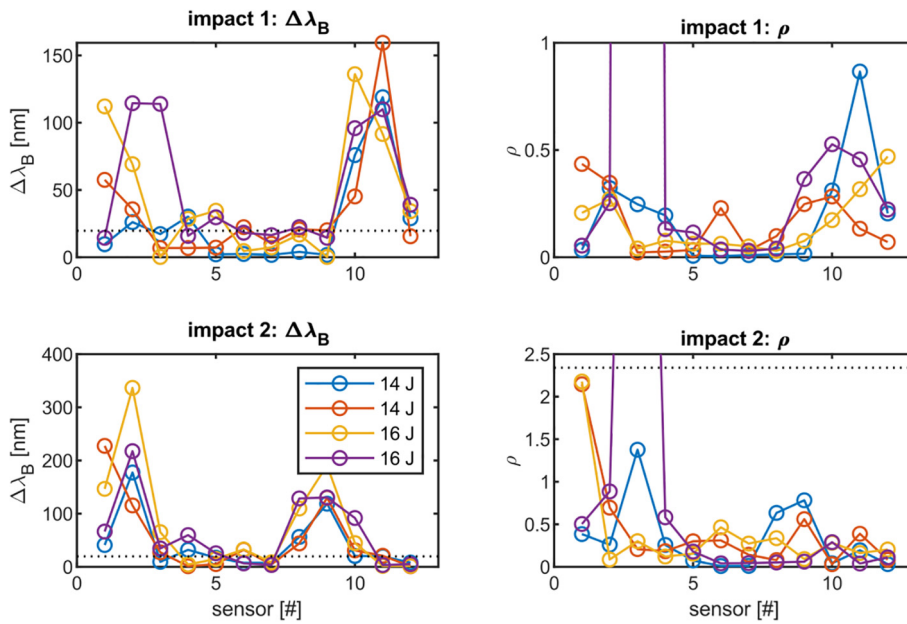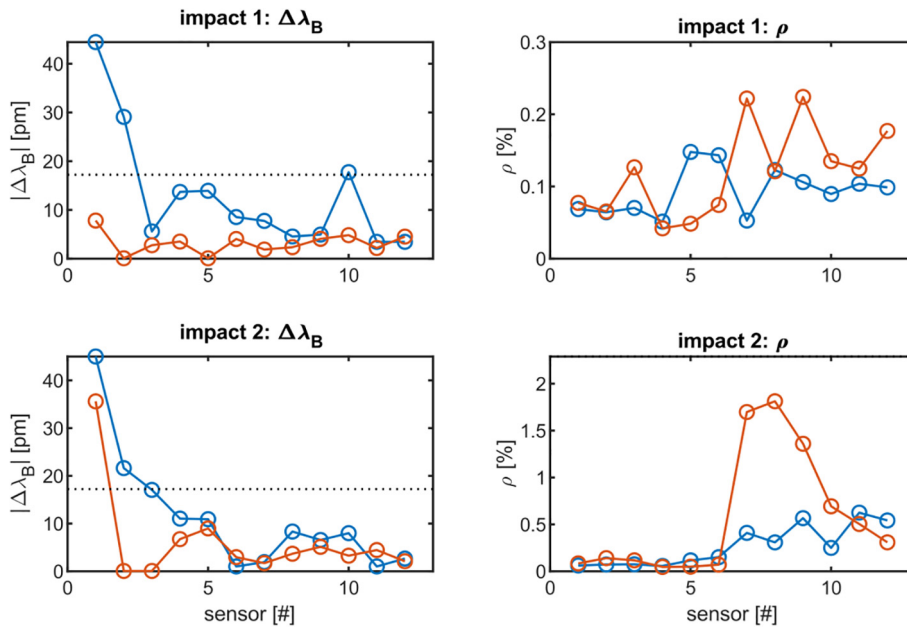
References

[1] Cawley P. The rapid non-destructive inspection of large composite structures. Composites 1994;25(5):351–7. https://doi.org/10.1016/S0010-4361(94)80005-7.

[2] Abbas S, Li F, Qiu J. A Review on SHM techniques and current challenges for characteristic investigation of damage in composite material components of aviation industry. Mater Perform Charact 2018;7(1):20170167. https://doi.org/10.1520/MPC20170167.

[3] Di Sante R. Fibre optic sensors for structural health monitoring of aircraft composite structures: recent advances and applications. Sensors 2015;15(8):18666–713. https://doi.org/10.3390/s150818666.

[4] Zhao G, Li S, Hu H, Zhong Y, Li K. Impact localization on composite laminates using fiber Bragg grating sensors and a novel technique based on strain amplitude. Opt Fiber Technol 2018;40:172–9. https://doi.org/10.1016/j.yofte.2017.12.001.

[5] Lamberti A, Luyckx G, Van Paepegem W, Rezayat A, Vanlanduit S. Detection, localization and quantification of impact events on a stiffened composite panel with embedded fiber Bragg grating sensor networks. Sensors 2017;17(4):743. https://doi.org/10.3390/s17040743.

[6] Takeda S-I, Aoki Y, Nagao Y. Damage monitoring of CFRP stiffened panels under compressive load using FBG sensors. Compos Struct 2012;94(3):813–9. https://doi.org/10.1016/j.compstruct.2011.02.020.

[7] Frieden J, Cugnoni J, Botsis J, Gmür T, Ćorić D. High-speed internal strain measurements in composite structures under dynamic load using embedded FBG sensors. Compos Struct 2010;92(8):1905–12. https://doi.org/10.1016/j.compstruct.2010.01.007.

[8] Vella T, Chadderdon S, Selfridge R, Schultz S, Webb S, Park C, Peters K, Zikry M. Full-spectrum interrogation of fiber Bragg gratings at 100 kHz for detection of impact loading. Meas Sci Technol 2010;21(9):094009. https://doi.org/10.1088/0957-0233/21/9/094009.

[9] Schultz S, Kunzler W, Zhu Z, Wirthlin M, Selfridge R, Propst A, Zikry M, Peters K. Full-spectrum interrogation of fiber Bragg grating sensors for dynamic measurements in composite laminates. Smart Mater Struct 2009;18(11):115015. https://doi.org/10.1088/0964-1726/18/11/115015.

[10] Tsutsui H, Kawamata A, Kimoto J, Sanda T, Takeda N, "Impact damage detection of curved stiffened composite panels by using wavy embedded small-diameter optical fibers," San Diego, CA, Jul. 2002, pp. 454–461, DOI: 10.1117/12.475090.

[11] Sai Y, Zhao X, Wang L, Hou D. Impact Localization of CFRP Structure Based on FBG Sensor Network. Photonic Sens 2020;10(1):88–96. https://doi.org/10.1007/s13320-019-0546-9.

[12] Datta A, Augustin MJ, Gupta N, Viswamurthy SR, Gaddikeri KM, Sundaram R. Impact localization and severity estimation on composite structure using fiber Bragg grating sensors by least square support vector regression. IEEE Sensors J 2019;19(12):4463–70. https://doi.org/10.1109/JSEN.2019.2901453.

[13] Jang B-W, Kim C-G. Impact localization of composite stiffened panel with triangulation method using normalized magnitudes of fiber optic sensor signals. Compos Struct 2019;211:522–9. https://doi.org/10.1016/j.compstruct.2019.01.028.

[14] Jang B-W, Kim C-G. Real-time detection of low-velocity impact-induced delamination onset in composite laminates for efficient management of structural health. Compos B Eng 2017;123:124–35. https://doi.org/10.1016/j.compositesb:2017.05.019.

[15] Shrestha P, Park Y, Kim C-G. Low velocity impact localization on composite wing structure using error outlier based algorithm and FBG sensors. Compos B Eng 2017;116:298–312. https://doi.org/10.1016/j.compositesb:2016.10.068.

[16] Rezayat A, De Pauw B, Lamberti A, El-Kafafy M, Nassiri V, Ertveldt J, Arroud G, Vanlanduit S, Guillaume P. Reconstruction of impacts on a composite plate using fiber Bragg gratings (FBG) and inverse methods. Compos Struct 2016;149:1–10. https://doi.org/10.1016/j.compstruct.2016.03.065.

[17] Shrestha P, Kim J-H, Park Y, Kim C-G. Impact localization on composite structure using FBG sensors and novel impact localization technique based on error outliers. Compos Struct 2016;142:263–71. https://doi.org/10.1016/j.compstruct.2016.01.088.

[18] Jang B-W, Kim C-G. Impact localization on a composite stiffened panel using reference signals with efficient training process. Compos B Eng 2016;94:271–85. https://doi.org/10.1016/j.compositesb:2016.03.063.

[19] Shrestha P, Kim J-H, Park Y, Kim C-G. Impact localization on composite wing using 1D array FBG sensor and RMS/correlation based reference database algorithm. Compos Struct 2015;125:159–69. https://doi.org/10.1016/j.compstruct.2015.01.029.

[20] Lu S, Jiang M, Sui Q, Sai Y, Jia L. Low velocity impact localization system of CFRP using fiber Bragg grating sensors. Opt Fiber Technol 2015;21:13–9. https://doi.org/10.1016/j.yofte.2014.07.003.

[21] Kim J-H, Kim Y-Y, Park Y, Kim C-G. Low-velocity impact localization in a stiffened composite panel using a normalized cross-correlation method. Smart Mater Struct 2015;24(4):045036. https://doi.org/10.1088/0964-1726/24/4/045036.

[22] Park CY, Kim JH, Jun S-M, Kim C-G. Localizations and force reconstruction of low-velocity impact in a composite panel using optical fiber sensors. Adv Compos Mater 2012;21(5-6):357–69. https://doi.org/10.1080/09243046.2012.736346.

[23] Frieden J, Cugnoni J, Botsis J, Gmür T. Low energy impact damage monitoring of composites using dynamic strain signals from FBG sensors – part I: impact detection and localization. Compos Struct 2012;94(2):438–45. https://doi.org/10.1016/j.compstruct.2011.08.003.

[24] Park CY, Jang B-W, Kim JH, Kim C-G, Jun S-M. Bird strike event monitoring in a composite UAV wing using high speed optical fiber sensing system. Compos Sci Technol 2012;72(4):498–505. https://doi.org/10.1016/j.compscitech.2011.12.008.

[25] Yashiro S, Wada J, Sakaida Y. A monitoring technique for disbond area in carbon fiber–reinforced polymer bonded joints using embedded fiber Bragg grating sensors: development and experimental validation. Struct Health Monit 2017;16(2):185–201. https://doi.org/10.1177/1475921716669979.

[26] Takeda S, Okabe Y, Takeda N. Monitoring of delamination growth in CFRP laminates using chirped FBG sensors. J Intell Mater Syst Struct 2008;19(4):437–44. https://doi.org/10.1177/1045389X06074085.

[27] Takeda S, Yamamoto T, Okabe Y, Takeda N. Debonding monitoring of composite repair patches using embedded small-diameter FBG sensors. Smart Mater Struct 2007;16(3):763–70. https://doi.org/10.1088/0964-1726/16/3/025.

[28] Takeda N, Okabe Y, Mizutani T. Damage detection in composites using optical fibre sensors. Proc Inst Mech Eng, Part G: J Aerospace Eng 2007;221(4):497–508. https://doi.org/10.1243/09544100JAERO148.

[29] Takeda S, Minakuchi S, Okabe Y, Takeda N. Delamination monitoring of laminated composites subjected to low-velocity impact using small-diameter FBG sensors. Compos A Appl Sci Manuf 2005;36(7):903–8. https://doi.org/10.1016/j.compositesa:2004.12.005.

[30] Okabe Y, Tsuji R, Takeda N. Application of chirped fiber Bragg grating sensors for identification of crack locations in composites. Compos A Appl Sci Manuf 2004;35(1):59–65. https://doi.org/10.1016/j.compositesa:2003.09.004.

[31] Takeda S, Okabe Y, Takeda N. Delamination detection in CFRP laminates with embedded small-diameter fiber Bragg grating sensors. Compos A Appl Sci Manuf 2002;33(7):971–80. https://doi.org/10.1016/S1359-835X(02)00036-2.

[32] Okabe Y, Mizutani T, Yashiro S, Takeda N. Detection of microscopic damages in composite laminates. Compos Sci Technol 2002;62(7-8):951–8. https://doi.org/10.1016/S0266-3538(02)00009-X.

[33] Peters K, Studer M, Botsis J, Iocco A, Limberger H, Salathé R. Embedded optical fiber Bragg grating sensor in a nonuniform strain field: measurements and simulations. Exp Mech 2001;41(1):19–28. https://doi.org/10.1007/BF02323100.

[34] Tsutsui H, Kawamata A, Sanda T, Takeda N. Detection of impact damage of stiffened composite panels using embedded small-diameter optical fibers. Smart Mater Struct 2004;13(6):1284–90. https://doi.org/10.1088/0964-1726/13/6/002.

[35] Choi B-H, Kwon I-B. Damage mapping using strain distribution of an optical fiber embedded in a composite cylinder after low-velocity impacts. Compos B Eng 2019;173:107009. https://doi.org/10.1016/j.compositesb:2019.107009.

[36] Batte LK, Sullivan RW, Ranatunga V, Brown K. Impact response in polymer composites from embedded optical fibers. J Compos Mater 2018;52(25):3415–27. https://doi.org/10.1177/0021998318763274.

[37] Yu F-M, Okabe Y, Wu Qi, Shigeta N. A novel method of identifying damage types in carbon fiber-reinforced plastic cross-ply laminates based on acoustic emission detection using a fiber-optic sensor. Compos Sci Technol 2016;135:116–22. https://doi.org/10.1016/j.compscitech.2016.09.017.

[38] Panopoulou A, Loutas T, Roulias D, Fransen S, Kostopoulos V. Dynamic fiber Bragg gratings based health monitoring system of composite aerospace structures. Acta Astronaut 2011;69(7-8):445–57. https://doi.org/10.1016/j.actaastro.2011.05.027.

[39] Mieloszyk M, Skarbek L, Krawczuk M, Ostachowicz W, Zak A. Application of fibre Bragg grating sensors for structural health monitoring of an adaptive wing. Smart Mater Struct 2011;20(12):125014. https://doi.org/10.1088/0964-1726/20/12/125014.

[40] Seaver M, Aktas E, Trickey ST. Quantitative detection of low energy impact damage in a sandwich composite wing. J Intell Mater Syst Struct 2010;21(3):297–308. https://doi.org/10.1177/1045389X09347020.

[41] Kim S-W. Effect of sensing distance of aluminum-coated FBG sensors installed on a composite plate under a low-velocity impact. Compos Struct 2017;160:248–55. https://doi.org/10.1016/j.compstruct.2016.10.050.

[42] Takeda S, Aoki Y, Ishikawa T, Takeda N, Kikukawa H. Structural health monitoring of composite wing structure during durability test. Compos Struct 2007;79(1):133–9. https://doi.org/10.1016/j.compstruct.2005.11.057.

[43] Goossens S, De Pauw B, Geernaert T, Salmanpour MS, Sharif Khodaei Z, Karachalios E, Saenz-Castillo D, Thienpont H, Berghmans F. Aerospace-grade surface mounted optical fibre strain sensor for structural health monitoring on composite structures evaluated against in-flight conditions. Smart Mater Struct 2019;28(6):065008. https://doi.org/10.1088/1361-665X/ab1458.

[44] "Hexcel." https://www.hexcel.com/ (accessed Nov. 26, 2019).

[45] "SAERTEX." https://www.saertex.com/en (accessed Nov. 26, 2019).

[46] "Solvay." https://www.solvay.com/en (accessed Nov. 26, 2019).

[47] "Teijin Carbon." https://www.teijincarbon.com/?r=1 (accessed Nov. 26, 2019).

[48] Johnson D, "Draw-tower process creates high-quality FBG arrays," Laser Focus World, vol. 48, pp. 53–56.

[49] Mihailov SJ. Fiber Bragg grating sensors for harsh environments. Sensors 2012;12(2):1898–918. https://doi.org/10.3390/s120201898.

[50] "FBGS international." https://fbgs.com/ (accessed Nov. 26, 2019).

[51] "HBM." https://www.hbm.com/en/ (accessed Nov. 26, 2019).

[52] Othonos A, "Bragg Gratings in Optical Fibers: Fundamentals and Applications," In Optical Fiber Sensor Technology: Advanced Applications — Bragg Gratings and Distributed Sensors, K. T. V. Grattan and B. T. Meggitt, Eds. Boston, MA: Springer US, 2000, pp. 79–187.

[53] Kashyap R. Fiber Bragg gratings. 2nd ed. Amsterdam: Elsevier/Acad. Press; 2010.

[54] Krohn DA, MacDougall T, Mendez A. Fiber optic sensors: fundamentals and applications. 4. ed. Bellingham, Wash: SPIE Press; 2014.

[55] "Santec." https://www.santec.com/en/ (accessed Nov. 26, 2019).

[56] "Thorlabs, Inc." https://www.thorlabs.com/ (accessed Nov. 26, 2019).

[57] "TiePie." https://www.tiepie.com/en (accessed Nov. 26, 2019).

[58] "Micron Optics." http://www.micronoptics.com/ (accessed Nov. 26, 2019).

[59] RTCA/DO-160, "Section 4.0 – Temperature and Altitude," DO160.org. https://do160.org/temperature-and-altitude/ (accessed Jul. 05, 2020).

[60] "TAS Ltd - Environmental Test Chambers for temperature & humidity generation and control." http://www.tasltd.co.uk/ (accessed Jul. 01, 2020).

[61] RTCA DO-160, "Section 8.0 – Vibration Test," DO160.org. https://do160.org/vibration/ (accessed Mar. 04, 2020).

[62] Gunawardena DS, Lai M-H, Lim K-S, Ahmad H. Thermal decay analysis of fiber Bragg gratings at different temperature annealing rates using demarcation energy approximation. Opt Fiber Technol 2017;34:16–9. https://doi.org/10.1016/j.yofte.2016.12.005.

[63] Erdogan T, Mizrahi V, Lemaire PJ, Monroe D. Decay of ultraviolet-induced fiber Bragg gratings. J Appl Phys 1994;76(1):73–80. https://doi.org/10.1063/1.357062.

[64] "Dolphitech Dolphicam," dolphitech. https://www.dolphitech.com/ (accessed Feb. 06, 2020).

[65] Goossens S et al., "Data for: Barely visible impact damage detection and location on aerospace-grade composite materials with in-flight compatible fibre Bragg grating sensors," Mendeley Data, vol. v1, 2020, DOI:10.17632/p858yck56r.1.